

Supplementary Information: Predicting the conductance of strongly correlated molecules: the Kondo effect in perchlorotriphenylmethyl/Au junctions

W. H. Appelt^{a,b}, A. Droghetti^c, L. Chioncel^{b,d}, M. M. Radonjić^e, E. Muñoz^f, S. Kirchner^g, D. Vollhardt^d, I. Rungger^{h,*}

^aTheoretical Physics II, Institute of Physics, University of Augsburg, D-86135 Augsburg, Germany

^bAugsburg Center for Innovative Technologies, University of Augsburg, D-86135 Augsburg, Germany

^cNano-Bio Spectroscopy Group and European Theoretical Spectroscopy Facility (ETSF), Centro de Física de Materiales, Universidad del País Vasco, Avenida Tolosa 72, 20018 San Sebastian, Spain

^dTheoretical Physics III, Center for Electronic Correlations and Magnetism, Institute of Physics, University of Augsburg, D-86135 Augsburg, Germany

^eScientific Computing Laboratory, Center for the Study of Complex Systems, Institute of Physics Belgrade, University of Belgrade, Pregrevica 118, 11080 Belgrade, Serbia

^fFacultad de Física, Pontificia Universidad Católica de Chile, Casilla 306, Santiago 22, Chile

^gZhejiang Institute of Modern Physics, Zhejiang University, Hangzhou, Zhejiang 310027, China

^hNational Physical Laboratory, Teddington, TW11 0LW, United Kingdom

* E-mail: ivan.rungger@npl.co.uk

S1 Computational details of the DFT and DFT+NEGF calculations

The DFT calculations in Sec. 2 of the main manuscript are performed with the pseudo-potential code SIESTA¹ and the all-electron code FHI-aims²⁻⁴. The computational details are the same as those used in previous works^{5,6}. For the gas phase molecule we use the Perdew-Burke-Ernzerhof (PBE) generalized gradient approximation (GGA)^{7,8} of the exchange-correlation functional, as well as the hybrid functional PBE0⁹. Additionally, the energy gaps in the density of states (DOS) are also computed with the spin-polarized G_0W_0 @PBE0 approximation of the many-body perturbation theory implemented in FHI-aims, and the results are presented in the Sec. S2. Geometry optimizations for the molecule integrated

into the Au electrodes are carried out with FHI-aims in a supercell approach and by employing the functional PBE+vdW^{surf}^{10,11}. The molecule and all the Au atoms, except for those at the boundary and those directly connected to leads in the transport setup, are allowed to relax until forces are smaller than 0.01 eV/Å.

DFT+NEGF calculations are performed with the *Smeagol* code^{12,13}. The geometries are obtained by joining the central part of the scattering region (optimized by using FHI-AIMS) to the Au electrodes, and all the considered structures are shown in Fig. 1 of the main manuscript. The simulation parameters for the DFT+NEGF calculations correspond to those outlined in Ref. 5. We employ non-spin-polarized DFT calculations, since the formation of either the local magnetic moment or the Kondo state is accounted for subsequently in the DFT+NEGF+NRG solu-

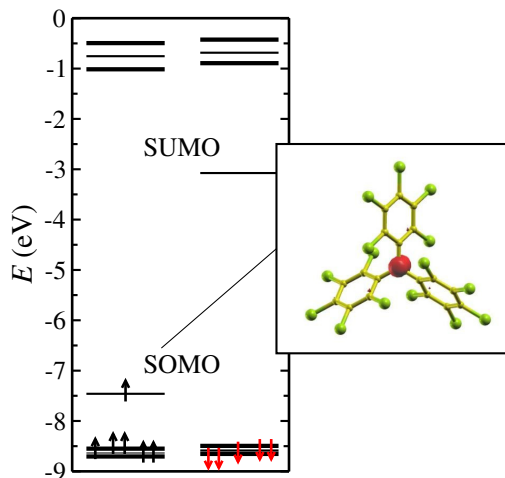


Figure S1 Highest occupied and lowest unoccupied molecular orbitals of the PTM radical computed with $G_0W_0@PBE0$. The SOMO and the SUMO are explicitly indicated. The SOMO-SUMO gap represents the gas phase charging energy U . Inset: charge isosurface for the SOMO (orange bubble); C atoms are in yellow, while Cl atoms are in light green.

tions. Results for a set of spinpolarized DFT+NEGF calculations are shown in Sec. S2.

S2 Spin-polarized DFT and DFT+NEGF calculations

The energy spectrum for the isolated PTM molecule for spin-polarized electrons is shown in Fig. S1. The calculations are performed by using $G_0W_0@PBE0$, which usually gives an accurate description of the energy levels of small molecules¹⁴. It can be seen that all spin-up and spin-down levels are occupied up to about -8.5 eV. At -7.5 eV there is an additional spin-up occupied state, the SOMO. The corresponding spin-down state is therefore empty, and its energy is separated by the charging energy $U = 4.31$ eV from that of the SOMO. This U value is in quite close agreement to the values obtained via finite energy difference calculations given in Sec. 2 of the main manuscript. Within the present spin-polarized picture, this empty down-spin state is usually called the singly unoccupied molecular orbital (SUMO). For energies above this state the spectrum is again approximately degenerate for up- and down-spins.

For the molecule adsorbed on the Au substrate we use DFT within the local spin-density approximation (LSDA) to compute the density of states (DOS), since $G_0W_0@PBE0$ becomes computationally too demanding. However, the LSDA DOS of the molecule suffers from the well-known DFT Kohn-Sham (KS) gap error. On the one hand, the

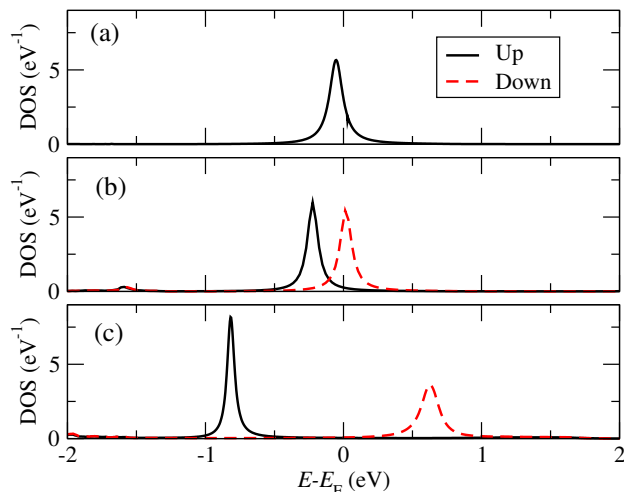


Figure S2 DOS of the PTM radical on Au for configuration B2 obtained within a) non-spinpolarized LDA, b) spin-polarized LDA, and c) spin-polarized LDA+SCO, with a correction energy of 1 eV.

KS SOMO-SUMO gap for the gas phase molecule is only about 0.4 eV, and is therefore significantly smaller than the $G_0W_0@PBE0$ result. This may lead to a drastic overestimation of the computed conductance. On the other hand, the SOMO-SUMO gap for molecules adsorbed on a metal substrate is known to shrink with respect to that in the gas phase due to the image charge effect^{15,16}. This effect is not captured by the KS description of the energy levels spectrum with local and semi-local functionals¹⁷⁻¹⁹. A fortuitous error cancellation between the gap underestimation and the neglect of image-charge effects may sometimes happen, but this is not generally the case and corrections are therefore needed.

A reliable estimate of the gap for adsorbed molecules is generally obtained from the gas phase value computed with G_0W_0 , to which one then adds a classical image-charge correction¹⁷⁻¹⁹. The practical way to adjust the gap in KS DFT-based electron transport calculations is then to add a scissor operator (SCO) correction to the KS eigenvalues²⁰⁻²³. In Fig. S2 (b)-(c) the DOS of the adsorbed molecule obtained without and with applying a scissor operator correction of 1 eV is shown, and compared also to the non-spinpolarized calculation in Fig. S2(a).

Note that while the SCO correction can move the SOMO and SUMO peaks to the correct energies, the DOS does not show any Kondo feature at E_F . Furthermore, magnetism in these DFT calculations is described by breaking the symmetry via the unequal occupation of spin up and spin down states²⁴. This does not correspond to the correct many-body picture, where the spin symmetry is preserved unless there is an external Zeeman field. The use of

KS-DFT with the SCO in transport is effectively equivalent to solving the SIAM in Eq. (1) with a static mean-field approximation^{5,25}. To obtain the correct Kondo physics and magnetic behavior it is necessary to add many-body corrections to the KS-DFT, for which we use the NRG in Sec. 3.3 of the main manuscript.

S3 Kondo temperature

The Kondo model is defined by the Hamiltonian

$$H_K = H_d + \frac{1}{2} J \vec{S}_d \sum_{k,k',\sigma,\sigma'} c_{k,\sigma}^\dagger \vec{\sigma}_{\sigma\sigma'} c_{k',\sigma'} \quad (\text{S1})$$

where $\vec{S}_d = \frac{1}{2} \sum_{\sigma\sigma'} d_\sigma^\dagger \vec{\sigma}_{\sigma\sigma'} d_{\sigma'}$ is the spin operator of the impurity site, the vector $\vec{\sigma}$ contains the Pauli-matrices as components, and J is a number representing an effective exchange coupling. As in Sec. 3.1 of the main manuscript, $c_{k,\sigma}$ ($c_{k,\sigma}^\dagger$) and d_σ (d_σ^\dagger) are the fermionic annihilation (creation) operators for the bath electrons and the impurity electrons, respectively. The SIAM in Eq. (1) maps onto the Kondo model under the following conditions. For a k -independent hybridization matrix element, $V_k = V$, a constant DOS of the bath, ρ , and therefore a constant $\Gamma = 2\pi V^2 \rho$, the impurity spin \vec{S}_d is coupled via $J = 2V^2 \left(\frac{1}{\varepsilon_d} - \frac{1}{\varepsilon_d + U} \right)$ to the bath²⁶. Note that the strong correlation limit ($U \gg \Gamma$) for the SIAM corresponds to the weakly coupled case in the Kondo model $J\rho \ll 1$.

A method to approach the so-called Kondo problem without employing perturbation theory or mean-field decoupling techniques was developed in a series of papers by Anderson and coworkers²⁷⁻³⁰, which then led to the renormalization group approach (RG) by Wilson³¹. In this method it became apparent that the generation of the low energy scale signals the renormalization group flow to a strong-coupling fixed point and a formation of a singlet state for temperatures $\theta \ll \theta_L$, where

$$\theta_L = \frac{1}{2} \sqrt{\Gamma U} e^{-\frac{1}{J\rho}}. \quad (\text{S2})$$

We can replace J and ρ by ε and Γ to obtain the equivalent equation (Ref. 32, page 168)

$$\theta_L = \frac{1}{2} \sqrt{\Gamma U} e^{\frac{\pi \varepsilon_d (\varepsilon_d + U)}{U\Gamma}}. \quad (\text{S3})$$

Since θ_L is defined by $\chi_s(\theta = 0) = (g\mu_B)^2 / 4k_B \theta_L$, it can be determined from the low-temperature limit of the magnetic susceptibility (see also page 155 in Ref. 32). For the half-filling case, where $\varepsilon_d = -U/2$, the temperature θ_L agrees with Wilson's numerical result up to a constant (the Wilson number)³³

$$c_W = \frac{\theta_W}{\theta_L} = 0.41072. \quad (\text{S4})$$

Here θ_W denotes the Kondo temperature deduced from the renormalization group calculations by Krishna-murthy *et al.*³⁴, which is equal to θ_L up to the scaling factor c_W .

S4 Computational details of the NRG calculations

The numerical renormalization group (NRG) method is a very powerful tool for the solution of effective impurity models³⁴⁻³⁹. The NRG is a non-perturbative approach and allows to access arbitrarily small energy scales, which is essential for the description of systems with characteristic temperatures of the order of 10K and below. NRG has been extended to handle arbitrary hybridization functions as input and allows one to produce dynamical quantities such as the impurity self-energy⁴⁰. In the present article we apply the recent methodological developments by Žitko⁴¹ in computing dynamical quantities, and we employ the z -averaging technique proposed by Oliveira and Oliveira⁴². Technical details for the application of the NRG to the Anderson model have been described in Ref. 37.

Here we only give a brief overview of the key steps to setup the NRG procedure. First, we divide the energy range of the bath spectral function into a set of logarithmic intervals, hence reducing the continuous spectrum to a discrete set of states (logarithmic discretization). The discretized version of the model Hamiltonian is mapped onto a one-dimensional system consisting of a semi-infinite chain of sites. The magnetic impurity, which is left unchanged by the unitary transformation, constitutes the first site in the semi-infinite chain. Only the coupling to the bath degrees of freedoms and the bath-geometry are modified. An iterative diagonalization of the impurity site, coupled to its adjacent bath site, is performed, where high energy levels are truncated. The truncation error can be controlled as long as the Hamiltonian parameters, like the on-site energies and couplings of adjacent sites along the chain, are well separated in energy. The separation of energy scales is guaranteed by the logarithmic discretization. The iterative diagonalization together with the rescaling of energies is understood as a mapping of the initial impurity site to an effective impurity site coupled to a bath with one bath site removed (the RG-step). Static thermodynamic and dynamic quantities can both be calculated from the knowledge of the energy spectrum and the eigenstates of the system. Care has to be taken, however, when one tries to analyze dynamical quantities, since the energy resolution is affected to some extent by the logarithmic discretization^{41,43}.

When temperature dependent quantities are computed in NRG, they are usually affected by truncation errors, since only a finite number of energy eigenvalues can be kept at each RG iteration. However, for thermodynamic

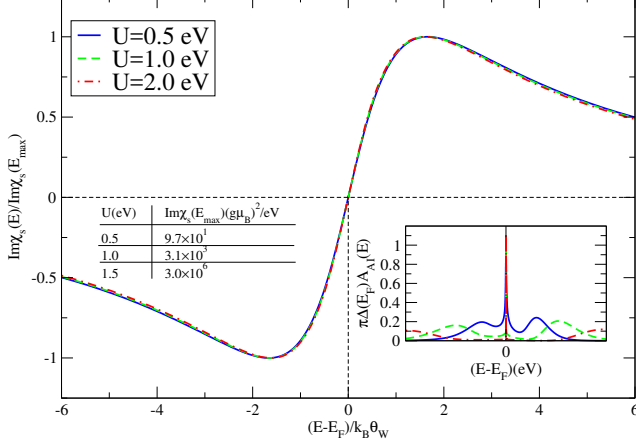


Figure S3 Dynamical spin susceptibility $\chi_s(E, \theta = 0)$ for different interaction strengths, calculated for hybridization function presented in Fig. 4 of the main manuscript, for configuration B4 (see Fig. 1 of the main manuscript), and $\theta = 0$ K. Inset: impurity density of states $A_{AI}(E)$. The calculation is performed close to the half-filled case.

quantities such as the impurity entropy, the specific heat and the susceptibility, one can show that the statistical weight of the truncated states is suppressed by the Boltzmann factor^{31,34,37,42}. We therefore use this scheme in order to compute the temperature dependence of the static susceptibility in Fig. 5 of the main manuscript. For dynamical quantities, such as the impurity spectral function, the situation is more complicated, since here the information of all energy scales enters. More elaborate schemes need to be employed in this case (see for example Ref. 37 and references therein).

We introduce an energy cutoff for the hybridization function. The left and right energy cutoffs are $[-1.20, 0.91]$ eV, $[-1.33, 0.30]$ eV, and $[-0.35, 0.80]$ eV for the B2, B4, and T4 configurations, respectively. From the truncated imaginary part we compute the real part by performing a Hilbert transformation. This procedure ensures that the analytic properties of $\Delta(\omega)$ are not modified due to the discretization and truncation. For large U it can be expected that the bandwidth of the conduction electrons is irrelevant for the low frequency behavior. The discretization scheme proposed in Ref. 44 is used, which corrects the systematic error in the first energy interval. The discretization parameter $\Lambda = 2$ is applied, and 5000 states are kept at each RG step.

S5 Impurity susceptibility

Here we derive the impurity contribution to the isothermal magnetic susceptibility, which is needed for accessing θ_w . It is closely related to the Matsubara susceptibility $\chi_n^s(\beta)$,

which is defined as (paramagnetic case):

$$\chi_n^s(\beta) = \int_0^\beta d\tau e^{i\omega_n\tau} \langle T_\tau S_{AI}^z(\tau) S_{AI}^z(0) \rangle. \quad (S5)$$

Here $S_{AI}^z(\tau)$ is the spin operator on the impurity site $S_{AI}^z = \frac{1}{2}(d_\uparrow^\dagger d_\uparrow - d_\downarrow^\dagger d_\downarrow)$ in the Heisenberg representation for imaginary times τ . We define the inverse temperature $\beta = 1/k_B\theta$, and denote with T_τ the time ordering operator, which moves the earlier times to the right. The brackets $\langle O \rangle$ on an operator O denote the thermodynamic average $\langle O \rangle = \text{Tr} [e^{-\beta(H-\mu N-\Omega)} O]$, with $e^{-\beta\Omega} = \text{Tr} [e^{-\beta(H-\mu N)}]$, where Ω is the grand canonical potential, μ is the chemical potential, and N is the particle number operator. We do not distinguish the Fermi energy E_F from the chemical potential μ in this article, and hence both are employed. The use of E_F is commonly used in the context of the first principles DFT-based calculations, while the chemical potential is favored in the context of statistical physics. The Matsubara frequencies are the complex energies $i\omega_n = i2n\pi/\beta$, where $n = 0, 1, 2, \dots$. The index n in Eq. S5 corresponds to the n -th Matsubara frequency. The isothermal magnetic susceptibility is given by the Matsubara susceptibility at the first Matsubara point $\chi_{n=0}^s(\beta)$. In the following we show how we calculate the isothermal magnetic susceptibility for finite temperatures. The total spin, projected on the z -direction, commutes with the Hamiltonian ($\langle S_{\text{tot}}^z(\tau) S_{\text{tot}}^z(0) \rangle = \langle (S_{\text{tot}}^z)^2 \rangle$) so that we find:

$$\chi_n^{\text{tot}}(\beta) = \int_0^\beta d\tau e^{i\omega_n\tau} \langle T_\tau S_{\text{tot}}^z(\tau) S_{\text{tot}}^z(0) \rangle \quad (S6)$$

$$\chi_{n=0}^{\text{tot}}(\beta) = \int_0^\beta d\tau \langle T_\tau S_{\text{tot}}^z(\tau) S_{\text{tot}}^z(0) \rangle \quad (S7)$$

$$= \beta \langle (S_{\text{tot}}^z)^2 \rangle, \quad (S8)$$

where $S_{\text{tot}}^z = \frac{1}{2}(d_\uparrow^\dagger d_\uparrow - d_\downarrow^\dagger d_\downarrow) + \frac{1}{2} \sum_k (c_{k,\uparrow}^\dagger d_{k,\uparrow} - d_{k,\downarrow}^\dagger d_{k,\downarrow})$. From Eq. (S8) one subtracts the susceptibility of a reference system, i.e. of the system without impurity $\chi_{n=0}^{(0),\text{tot}}(\beta)$. This gives Wilson's definition of the impurity contribution to the susceptibility^{31,37}:

$$\chi_s(\beta) \equiv \chi_{n=0}^s(\beta) = \chi_{n=0}^{\text{tot}}(\beta) - \chi_{n=0}^{(0),\text{tot}}(\beta). \quad (S9)$$

The latter is used to determine the Kondo scaling.

The dynamical spin susceptibility is defined as⁴⁵:

$$\chi_s(E, \beta) = i \int_{-\infty}^0 dt e^{iEt} \langle [S_{AI}^z(t), S_{AI}^z(0)] \rangle, \quad (S10)$$

where $S_{AI}^z(t)$ is spin operator on the impurity site, $S_{AI}^z = \frac{1}{2}(d_\uparrow^\dagger d_\uparrow - d_\downarrow^\dagger d_\downarrow)$, in the Heisenberg representation for real times t . The susceptibilities in Eq. S10 and Eq. S5 are related by analytic continuation $i\omega_n \rightarrow E + i\eta$. In

Fig. S3 we show the imaginary part of $\chi_s(E, \theta = 0)$ at zero temperature, and the inset shows the density of states $A_{\text{AI}}(E) = -\frac{1}{\pi} \text{Im} G_{d\sigma, d\sigma}(E)$ of the impurity site, where $G_{d\sigma, d\sigma}(E) = -i \int_{-\infty}^0 dt e^{iEt} \langle [d_\sigma(t), d_\sigma^\dagger(0)] \rangle$ is the one-electron Green's function on the impurity site. A clear three-peak structure is found which is characteristic for the SIAM. In particular, the low-energy physics is described by a Kondo resonance in the DOS around $E = E_F = 0$, which is gradually suppressed upon increasing U (not shown). The atomic levels, broadened by the coupling to the conducting electrons, are located at $\varepsilon_d \pm U/2$. The energy axis of $\text{Im}\chi_s(E, \theta = 0)$ is scaled by θ_W , which is determined from the impurity contribution to the isothermal magnetic susceptibility $\chi_s(0, \theta = 0)$ defined above. One can clearly see that the $\text{Im}\chi_s(E, \theta = 0)$ reaches a minimum (maximum) around $(E - E_F)/\theta_W \approx 1$ (around $(E - E_F)/\theta_W \approx -1$). The vertical axis is scaled by the maximum value of $\text{Im}\chi_s(E, \theta = 0)$, denoted by $\text{Im}\chi_s(E_{\text{max}}, \theta = 0)$, as given in the table in Fig. S3.

S6 Full width at half maximum of the Kondo peak

For a non-spinpolarized system the temperature dependent spin-resolved spectral function $A_{\text{AI}} = A_{\text{AI}}^\uparrow = A_{\text{AI}}^\downarrow$ of the SIAM is given by

$$A_{\text{AI}}(E, \theta) = \frac{1}{\pi} \frac{\Delta - \text{Im}(\Sigma(E, \theta))}{[E - \varepsilon_d - \text{Re}(\Sigma(E, \theta))]^2 + [\Delta - \text{Im}(\Sigma(E, \theta))]^2}, \quad (\text{S11})$$

with $\Delta = \Gamma/2$ and ε_d defined in the main text. The normalization of $A_{\text{AI}}(E, \theta)$ is chosen in such a way that $\int_{-\infty}^{\infty} A_{\text{AI}}(E, \theta) dE = 1$, so that it is equal to the density of states. Here Δ is assumed to be energy-independent, and we will discuss the implication of this approximation in the following. The low-energy behavior of A_{AI} is then determined by the low energy expansion of the many-body SIAM self-energy $\Sigma(E, \theta)$. In the half-filled, strong correlation ($\Delta \ll U$) case considered here we have $\varepsilon_d + \text{Re}(\Sigma(0, 0)) = 0$, so that A_{AI} is particle-hole symmetric for a constant Δ . In this case, the zero voltage low energy expansion of $\Sigma(E, \theta)$ for real energies E is given by⁴⁷⁻⁴⁹

$$\Sigma(E, \theta) \approx -\varepsilon_d + (1 - z^{-1})E - i\frac{\Delta}{2} \left(\frac{E^2}{\tilde{\Delta}^2} + \frac{\pi^2 k_B^2 \theta^2}{\tilde{\Delta}^2} \right), \quad (\text{S12})$$

with $\tilde{\Delta} = z\Delta = z\Gamma/2$, and $z = (1 - \frac{\partial \text{Re}(\Sigma(E))}{\partial E} |_{E=0})^{-1}$, evaluated at zero temperature^{47,48}. We now insert Eq. (S12) into Eq. (S11), and find that A_{AI} is maximal at $E = 0$, with the

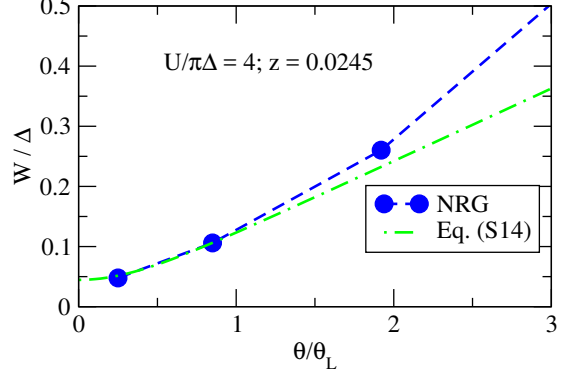


Figure S4 Comparison of the results for the full width at half maximum, W , of the Kondo peak as function of temperature, obtained by NRG and by the approximated relation in Eq. (S14) respectively. The NRG results are extracted from Fig. 6 of Ref. 49. The parameters used in the NRG calculations are $U/\pi\Delta = 4$, and a constant DOS of the electrodes as function of energy is assumed.

height of the peak given by

$$A_{\text{AI}}(0, \theta) = \frac{1}{\pi\Delta} \frac{1}{1 + \frac{\pi^2 k_B^2 \theta^2}{2\tilde{\Delta}^2}}. \quad (\text{S13})$$

The full width at half maximum, W , is determined by solving the condition $A_{\text{AI}}(W/2, \theta) = A_{\text{AI}}(0, \theta)/2$ for W . Using Eqs. (S11-S13) one then obtains

$$W(\theta, \tilde{\Delta}) = \tilde{\Delta} 2\sqrt{2} \sqrt{\sqrt{1 + \left(\frac{\pi^2 k_B^2 \theta^2}{2\tilde{\Delta}^2} + 1 \right)^2} - 1}. \quad (\text{S14})$$

At zero temperature this FWHM is

$$W(0, \tilde{\Delta}) = \tilde{\Delta} 2\sqrt{2} \sqrt{\sqrt{2} - 1}. \quad (\text{S15})$$

To estimate the validity of our approximation in Eq. (S14) for $W(\theta, \tilde{\Delta})$, in Fig. S4 we compare it to the exact results obtained from NRG calculations in Ref. 49. The agreement is very good up to about $\theta \approx 2\theta_L$, above which the NRG FWHM rises faster. This is mainly due to the fact that in our approximation we assume that there is only the Kondo peak, while in the full spectral function also the two side-peaks at $\pm U/2$ contribute to the spectral function around $E \approx 0$. This contribution increases relative to the height of the Kondo peak as the temperature increases well above θ_L .

We can now apply Eq. (S14) for the FWHM to our Au-PTM system. We first fit $\Sigma(E, 0)$ calculated using the NRG to the expansion in Eq. (S12) by adjusting the free parameters in that equation, namely z and Δ at zero temperature.

Configuration	z_Σ	Δ_Σ (meV)	$\tilde{\Delta}_\Sigma$ (meV)	W_Σ (meV)	W_{Ref} (meV)	$\Delta = \frac{\Gamma}{2}$ (meV)	W_T (meV)
B2	0.00315	67	0.210	0.381	0.599	57	0.381
B4	0.00326	67	0.215	0.395	0.612	59	0.408
T4	0.00598	75	0.449	0.816	1.265	63	0.830

Table S1 Values of z_Σ and Δ_Σ extracted from the low-energy many-body self-energy (Eq. (S12)), and resulting FWHM W_Σ at zero temperature using Eq. (S15), are compared to the values for $\Delta = \Gamma/2$ obtained directly from the DFT calculations (see Fig. 1 of the main manuscript) and of the FWHM obtained from the width of the Kondo peak in the transmission coefficients, W_T . We also present the value obtained from $\tilde{\Delta}_\Sigma$ using the relation given in Ref. 46, denoted as W_{Ref} .

We denote these fitted values as z_Σ and Δ_Σ ($\tilde{\Delta}_\Sigma = z_\Sigma \Delta_\Sigma$), and the zero temperature FWHM calculated with these values in Eq. (S15) as W_Σ . The resulting values are given in Table S1, where we also compare them with $\Delta = \Gamma/2$ extracted from the DFT calculations (see Fig. 1 of the main manuscript), and to the FWHM evaluated directly from the width of the transmission peaks in Fig. 6 of the main manuscript, which we denote as W_T . One can see that Δ_Σ and Δ are in rather good agreement, confirming the validity of the expansion in Eq. (S12) for our system. Since the hybridization function of the Au-PTM system is energy dependent, we can interpret the fitted values Δ_Σ as effective average hybridization strengths. In the same way z_Σ corresponds to an effective average wave-function renormalization factor, and $\tilde{\Delta}_\Sigma$ to an effective renormalized hybridization. These therefore correspond to the effective NRG results for z and $\tilde{\Delta}$, and we report them in Table 1 of the main manuscript. Importantly, W_Σ and W_T are also in good agreement, confirming the validity of the relations presented in this appendix. We note that in Ref. 50 the zero temperature FWHM is given by a different relation, which we denote as W_{Ref} , namely $W_{\text{Ref}} = 2\tilde{\Delta}\sqrt{2}$. Using our fitted values of $\tilde{\Delta}_\Sigma$ we also evaluate W_{Ref} for all configurations, and the values are reported in Table S1. One can see that W_{Ref} systematically overestimates the FWHM when compared to the correct value W_T . This is in contrast to W_Σ , which agrees well with W_T , showing that our expansion in Eq. (S14) provides a more accurate approximation of the Kondo peak width.

S7 Transmission, current and conductance

In the case of the SIAM, the total current can be written as⁵

$$I = 2\frac{e}{h} \int dE (f_L(E) - f_R(E)) T_t(E), \quad (\text{S16})$$

where $f_{L(R)}(E) = f(E - \mu_{L(R)})$ is the Fermi function of the left (right) electrode with chemical potential $\mu_{L(R)}$, $T_t(E) = T_t^\uparrow(E) = T_t^\downarrow(E)$ is the spin-resolved total effective transmission, and the factor 2 takes into account the spin-degeneracy. The applied bias voltage, V , is equal to $V =$

$(\mu_L - \mu_R)/e$, and $T_t(E)$ is given by

$$T_t(E) = T_B(E) + T_{\text{AI}}(E) + T_I(E) + T_{\text{R,AI}}(E), \quad (\text{S17})$$

and includes elastic and incoherent transmission through the impurity, $T_I(E)$ and $T_{\text{R,AI}}(E)$, as well as the background transmission $T_B(E)$ and the interference term $T_I(E)$. The total elastic transmission is $T(E) = T_{\text{AI}}(E) + T_B(E) + T_I(E)$. The effective total transmission $T_{t,\text{AI}}(E)$ through the impurity can be written as⁵¹

$$\begin{aligned} T_{t,\text{AI}}(E) &= T_{\text{AI}}(E) + T_{\text{R,AI}}(E) \\ &= 2\pi \frac{\Gamma_L(E)\Gamma_R(E)}{\Gamma_L(E) + \Gamma_R(E)} A_{\text{AI}}(E). \end{aligned} \quad (\text{S18})$$

Here it is assumed that $\Gamma_L(E) = \lambda \Gamma_R(E)$, with λ a constant. In Figs. S5-S7 we present $T(E)$ and $T_t(E)$ for different values of U . The configurations correspond to the ones described in the main text, namely B2, B4, and T4 (see Fig. 6 of the main manuscript). Note that these are all results for $\theta = 0$, so that $T(E_F) = T_t(E_F)$, and moreover the Kondo peak width becomes vanishingly small as U becomes large.

We can split the total current according to the different contributions in the transmission as

$$I = I_{\text{AI}} + I_B + I_I, \quad (\text{S19})$$

where

$$I_{\text{AI}} = \frac{2e}{h} \int dE (f_L(E) - f_R(E)) T_{t,\text{AI}}(E), \quad (\text{S20})$$

$$I_I = 2\frac{e}{h} \int dE (f_L(E) - f_R(E)) T_I(E), \quad (\text{S21})$$

$$I_B = 2\frac{e}{h} \int dE (f_L(E) - f_R(E)) T_B(E). \quad (\text{S22})$$

Note that the transmission coefficients in this set of equations depend also on μ_L and μ_R . In an analogous way we then split the total conductance in its individual contributions

$$G = G_{\text{AI}} + G_B + G_I, \quad (\text{S23})$$

with $G_{\text{AI}} = dI_{\text{AI}}/dV$, $G_I = dI_I/dV$, and $G_B = dI_B/dV$.

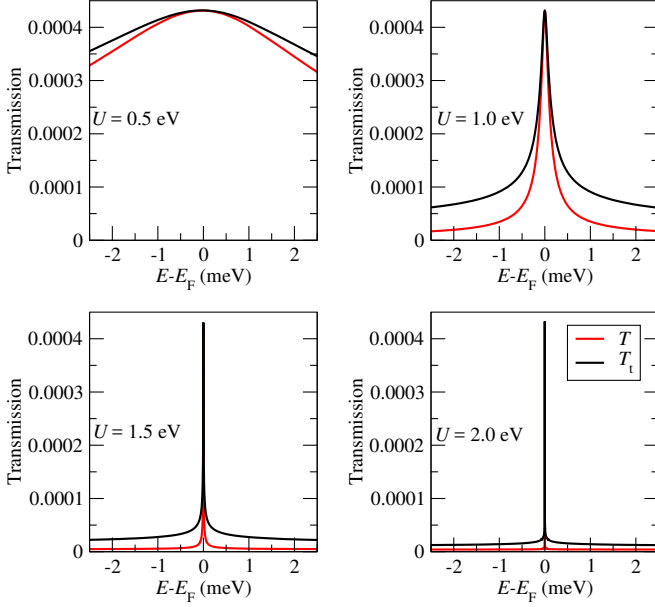


Figure S5 Transmission including the NRG self-energy for the B2 structure, for four different values of U .

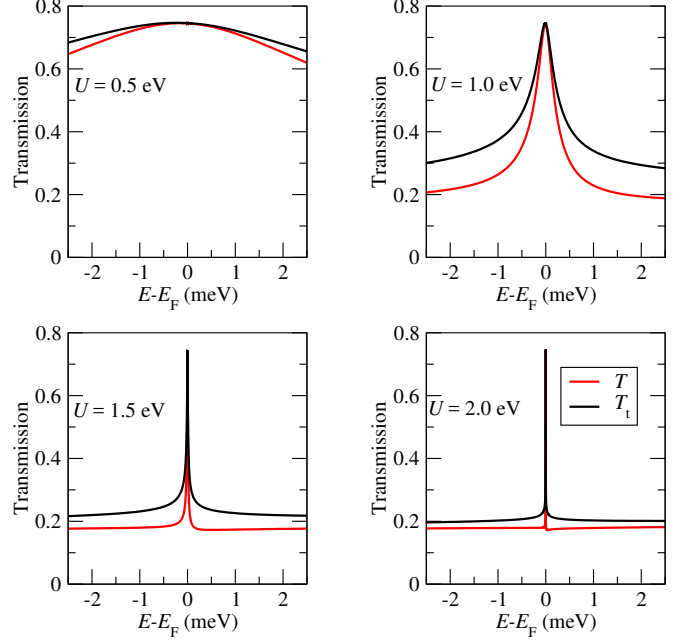


Figure S7 Transmission including the NRG self-energy for the T4 structure, for four different values of U .

S8 Conductance of the Kondo resonance

S8.1 Low voltage and temperature expansion

For a finite applied bias voltage the low energy expansion of the many-body self-energy contains additional voltage dependent terms when compared to Eq. (S12), as discussed in Ref. 48. However, if one considers the highly asymmetric case, where $\Gamma_L \gg \Gamma_R$ or $\Gamma_R \gg \Gamma_L$, these terms vanish. The SIAM spectral function is then independent of the voltage, except for a rigid shift along the energy axis, which is set by the choice of the arbitrary constant potential shift that can be applied to the whole system. The physical origin of this behaviour can be explained as follows: if either one of Γ_L or Γ_R is very small, then the current through the system is also small, so that the change in the shape of the spectral function with applied voltage is negligible. Without loss of generality we then set the rigid shift of the spectral function to be 0, which is obtained by setting $\mu_L = E_F$ and $\mu_R = E_F - eV$ when $\Gamma_L \gg \Gamma_R$, and by setting $\mu_L = E_F + eV$ and $\mu_R = E_F$ when $\Gamma_R \gg \Gamma_L$. In the following we only consider the case $\Gamma_L \gg \Gamma_R$, the equations for $\Gamma_R \gg \Gamma_L$ can be obtained in an analogous way. With this system setup, and with E_F set to 0, for $\Gamma_L \gg \Gamma_R$ the conductance of the AI as function of the applied bias,

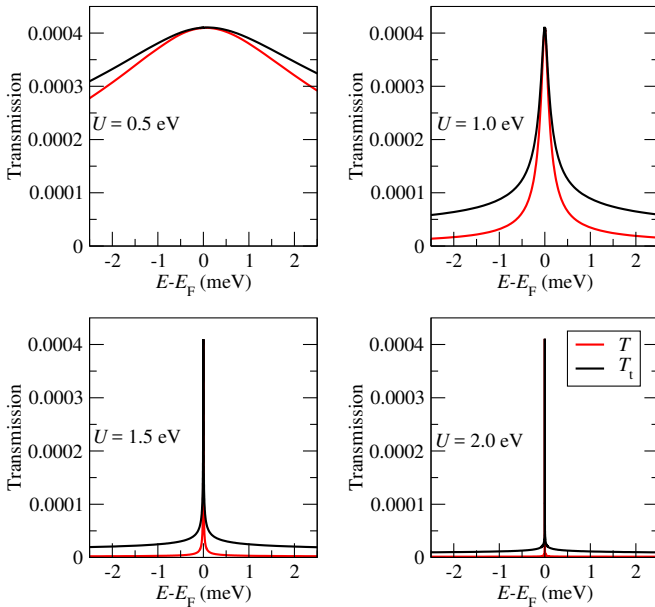


Figure S6 Transmission including the NRG self-energy for the B4 structure, for four different values of U .

$G_{\text{AI}}(V, \theta) = dI_{\text{AI}}/dV$, results from Eq. (S20) to

$$G_{\text{AI}}(V, \theta) \approx -\frac{2e^2}{h} \int T_{\text{t,AI}}(E - eV, \theta) \frac{df(E)}{dE}. \quad (\text{S24})$$

At zero temperature $G_{\text{AI}}(V, \theta = 0) \approx (2e^2/h)T_{\text{t,AI}}(-eV, \theta = 0)$. At finite low temperatures we can perform a Sommerfeld expansion of the energy integral involved in the calculation of the current, and to second order in θ the conductance then becomes

$$G_{\text{AI}}(V, \theta) \approx \frac{2e^2}{h} [T_{\text{t,AI}}(-eV, \theta) + \frac{\pi^2}{6} \left. \frac{\partial^2 T_{\text{t,AI}}(E, \theta)}{\partial E^2} \right|_{E=-eV} k_{\text{B}}^2 \theta^2]. \quad (\text{S25})$$

Using Eq. (S18) the temperature dependent $T_{\text{t,AI}}(E, \theta)$ can be rewritten as $T_{\text{t,AI}}(E, \theta) = 2\pi[\Gamma_{\text{L}}\Gamma_{\text{R}}/(\Gamma_{\text{L}} + \Gamma_{\text{R}})]A_{\text{AI}}(E, \theta)$. With Eqs. (S11) and (S12) we can then expand $T_{\text{t,AI}}(E = -eV, \theta)$ to lowest order in powers of V and θ , and obtain

$$T_{\text{t,AI}}(E = -eV, \theta) \approx \frac{\Gamma_{\text{L}}\Gamma_{\text{R}}}{\Gamma_{\text{L}} + \Gamma_{\text{R}}} \frac{2}{\Delta} \left[1 - \frac{3}{2} \frac{e^2 V^2}{\tilde{\Delta}^2} - \frac{\pi^2}{2} \frac{k_{\text{B}}^2 \theta^2}{\tilde{\Delta}^2} \right], \quad (\text{S26})$$

and

$$\frac{\pi^2}{6} \left. \frac{\partial^2 T_{\text{t,AI}}(E, \theta)}{\partial E^2} \right|_{E=-eV} k_{\text{B}}^2 \theta^2 \approx \frac{\Gamma_{\text{L}}\Gamma_{\text{R}}}{\Gamma_{\text{L}} + \Gamma_{\text{R}}} \frac{2}{\Delta} \left[-\frac{\pi^2}{2} \frac{k_{\text{B}}^2 \theta^2}{\tilde{\Delta}^2} \right], \quad (\text{S27})$$

If we insert these last two equations into Eq. (S25) we obtain

$$G_0 = G_{\text{AI}}(0, 0) = \frac{2e^2}{h} \frac{4\Gamma_{\text{L}}\Gamma_{\text{R}}}{(\Gamma_{\text{L}} + \Gamma_{\text{R}})^2}, \quad (\text{S28})$$

and

$$\frac{G_{\text{AI}}(V, \theta) - G_0}{G_0} \approx -\frac{3}{2} \frac{e^2 V^2}{\tilde{\Delta}^2} - \pi^2 \frac{k_{\text{B}}^2 \theta^2}{\tilde{\Delta}^2}, \quad (\text{S29})$$

and from this relation we can directly extract the lowest order expansion coefficients of the conductance (see Eq. (14) of the main manuscript) as

$$c_V = \frac{3}{2}, \quad (\text{S30})$$

$$c_\theta = \pi^2. \quad (\text{S31})$$

These results are valid in the strong correlation limit ($U \gg \Gamma$) and at particle-hole symmetry, and agree with the general values obtained in Ref. 48,52 and in Sec. S9 for this case. We note that the full energy dependent transmission contains more information than this lowest order expansion, which is valid only in the low voltage region.

S8.2 Approximations for large temperatures

As voltages or temperatures get large, the second order expansion discussed so far will eventually deviate significantly from the correct result, and we now estimate the magnitude of the voltages and temperatures at which this happens.

By comparing the exact NRG results for $\Sigma(E, 0)$ to the second order expansion (Eq. (S12)) we find that the terms describing the energy dependence are approximately valid for energies also beyond $\tilde{\Delta}$, so that they are rather well suited to describe the shape of the Kondo peak at zero temperature. This is also reflected in the fact that the second order expansion of the FWHM of the Kondo Peak agrees well with the exact NRG results (see Fig. S4).

To separately verify the range of validity of the second order expansion in temperature of the self-energy we evaluate $A_{\text{AI}}(0, \theta)$ (Eq. (S11)) for increasing temperatures using the second order expansion of $\Sigma(0, \theta)$ given in Eq. (S12), and then compare it to the exact NRG results of Ref. 49. This comparison is presented in Fig. S8(a), where we plot the normalized spectral function $A_{\text{AI}}(0, \theta)/A_{\text{AI}}(0, 0)$ as function of temperature, and the green dash-dotted curve is the result of the second order expansion, while the large blue dots are the exact NRG data. It can be seen that the results agree well for low θ , and that even at higher θ they qualitative behaviour of a decaying height of the Kondo peak is captured by the second order expansion. On a quantitative level however the results start to deviate significantly already at temperatures of about $0.5 \theta_{\text{L}}$, with the second order expansion results overestimating the decay.

In analogy of the second order expansion of the conductance presented in the previous subsection (Eq. S29) we now also expand $A_{\text{AI}}(0, \theta)$ to second order in θ . Using Eqs. (S11) and (S12) we obtain

$$A_{\text{AI}}(E = 0, \theta) = \frac{1}{\pi\Delta} \left[1 - \frac{1}{2} \pi^2 \frac{k_{\text{B}}^2 \theta^2}{\tilde{\Delta}^2} + O\left(\frac{k_{\text{B}} \theta^4}{\tilde{\Delta}^4}\right) \right], \quad (\text{S32})$$

with the second order coefficient $\pi^2/2$ equal to half the size of the second order temperature expansion coefficient for the conductance, c_T , given in Eq. (S31). The larger size of c_T is due to the fact that additionally to the change in $A_{\text{AI}}(E = 0, \theta)$ it also captures the temperature induced broadening of the Fermi distribution. Overall we can then expect that the range of validity in terms of magnitude of temperature is similar for $A_{\text{AI}}(E = 0, \theta)$ and for the 0 bias conductance $G(V = 0, \theta)$.

We can equivalently express the expansion of $A_{\text{AI}}(E = 0, \theta)$ directly in terms of $k_{\text{B}} \theta_{\text{L}} = \frac{\pi}{4} \tilde{\Delta}$ [Eq. (8) of the main manuscript] as

$$A_{\text{AI}}(E = 0, \theta) = \frac{1}{\pi\Delta} \left[1 - \frac{1}{2} \left(\frac{\pi}{2}\right)^4 \frac{\theta^2}{\theta_{\text{L}}^2} + O\left(\frac{\theta^4}{\theta_{\text{L}}^4}\right) \right]. \quad (\text{S33})$$

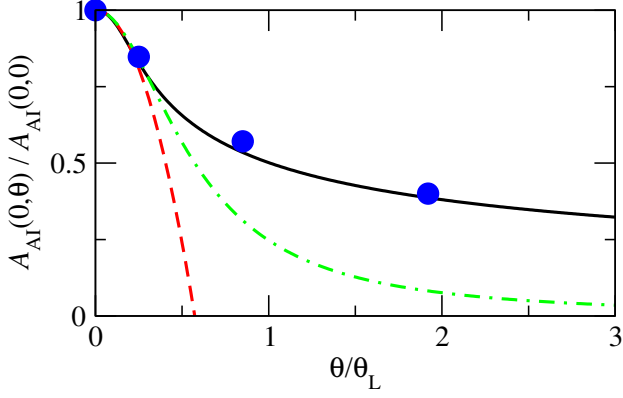


Figure S8 Temperature dependent normalized density of states, equivalent to the spectral function, as function of temperature; the NRG results (blue filled circles) are extracted from Fig. 6 in Ref. 49. The green dash-dotted lines correspond to the relation given in Eq. (S13), the red dashed curve indicates the exact second order low temperature expansion in Eq. (S33), and the black curve shows the DOS fitted to the NRG results using Eq. (S35).

The results are plotted as red dashed curve in Fig. S8. It can be seen that this expansion starts to significantly deviate from the exact NRG results already at about $\theta \approx 0.2\theta_L$. Since we expect a similar upper limit of the validity for temperature dependent zero-bias conductance, it shows that to reliably compare experiment to the second order expansion in Eqs. (14) of the main manuscript, or (S29), accurate measurements are needed for temperatures smaller than about $0.2\theta_L$.

In practice it is difficult to accurately measure the conductance below $0.2\theta_L$, and indeed most experiments measure up to temperatures significantly larger than θ_L . Therefore, based on the exact NRG results in⁴⁹ a fitting function for the temperature dependent low bias conductance has been proposed in Ref. 53, which has then been found to match well the experimental conductance drop with temperature. The form of this fitting function is

$$G(V=0, \theta) = G_0 \left[1 + a \frac{\theta^2}{\theta_L^2} \right]^{-s} + G_B, \quad (\text{S34})$$

with G_B equal to the background conductance, $G_0 = G(V=0, \theta=0) - G_B$, and with a determined by the imposed condition that $G(0, \theta_{L,1/2}) = 1/2$. Note that $\theta_{L,1/2}$ is similar but not identical to θ_L . For large U/Γ , as is the case for the AuPTM system, the value is given as $1.2\theta_L$ in Ref. 49 and as $1.041\theta_L$ in Ref. 54. If we neglect this small difference and assume $\theta_{L,1/2} \approx \theta_L$, then we obtain $a = 2^{1/s} - 1$. We then determine the value of s from the condition that the second order expansion in θ of Eq. (S34) has to correspond

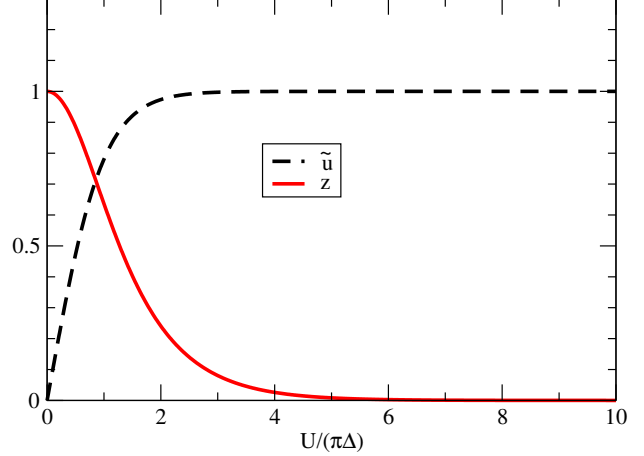


Figure S9 The Bethe ansatz results for the wave function renormalization factor, z , and the rescaled interaction \tilde{u} , as defined in Sec. 5 of the main manuscript. Note that the strong coupling fixed point value $\tilde{u} = 1$ is already reached for $U/(\pi\Delta) \approx 2$.

to the exact result in Eq. (S29), which gives the relation $s(2^{1/s} - 1) = (\pi/2)^4$. This can be solved numerically to give $s \approx 0.20$.

In order to obtain an empirical equation for the temperature dependence of the self-energy we now use an analogous approach to fit NRG results of $A_{AI}(E=0, \theta)$ for the whole temperature range shown in Fig. S8(a). Based on the empirical fitting Eq. (S34) for the conductance we use a similar functional form to fit $A_{AI}(0, \theta)$ to the NRG results:

$$A_{AI}(E=0, \theta) = \frac{1}{\pi\Delta} \left[1 + a \frac{\theta^2}{\theta_L^2} + \left(a \frac{\theta^2}{\theta_L^2} \right)^2 \right]^{-s/2}, \quad (\text{S35})$$

where a and s have the same values as used in Eq. (S34). The resulting function is shown as black curve in Fig. S8(a), and it can be seen that it approximates well the exact NRG results. It is also straight forward to verify that this fitting function has the correct second order expansion given in Eq. (S33).

S9 Expansion coefficients of the rSPT conductance

In this section, we provide full expressions for all transport coefficients, defined in Eq. (14) of the main manuscript. The results are based on the extended version of the rSPT, introduced in reference⁵⁵ but have not been presented previously. As a result, the transport coefficients below are correct to higher order in the deviation from the symmetric Anderson model than those in⁴⁸. As discussed in section 5 of the main manuscript, the central object of the method is the wavefunction renormalization factor z . For a constant

hybridization function, it can be obtained exactly via the Bethe ansatz⁴⁸. Fig. S9 shows z and \tilde{u} obtained from the Bethe ansatz as a function of the bare Coulomb interaction U , measured in units of $\pi\Delta$.

For an energy-dependent hybridization function, the NRG can be used to obtain z through $z = (1 - \partial\Sigma_\sigma^R(\omega)|_{\omega=0})^{-1}$ as discussed in the main part. Alternatively, z can also be determined perturbatively through

$$z = 1 + \frac{\tilde{U}^2}{2} \int_{-\infty}^{+\infty} \frac{d\omega}{2\pi i} \left[\tilde{\Pi}^{(0)A}(-\omega) \frac{\partial}{\partial\omega} \tilde{g}^{(0)K}(\omega) + \tilde{\Pi}^{(0)K}(-\omega) \frac{\partial}{\partial\omega} \tilde{g}^{(0)R}(\omega) \right] + O(\tilde{U}^3), \quad (\text{S36})$$

here $\tilde{U} = z^2\Gamma_{\uparrow\downarrow}(0,0,0,0)$, where $\Gamma_{\uparrow\downarrow}(0,0,0,0)$ is the two-particle vertex of the reference system at $\omega = 0, \theta = 0, V = 0$. Then, at the order of approximation used in the underlying expansion, it turns out that $\Gamma_{\uparrow\downarrow}(0,0,0,0) = U + O(U^3)$, and hence up to second order one has $\tilde{U} \sim z^2U + O(U^3)$; $\tilde{g}^{(0)x}$ is the renormalized Green function, and $\tilde{\Pi}^{(0)x}$ refers to the renormalized polarization bubble of the reference system, *i.e.*, where $2\varepsilon_d + U = 0$, indicated by the superscript (0) and $x = K, A, R$ denotes the Keldysh, advanced, retarded

component respectively. All terms in Eq. (S36) have to be evaluated in the zero-temperature ($\theta = 0$) limit. In the case of a constant hybridization function, this equation reduces to

$$2\left(3 - \frac{\pi^2}{4}\right)\left(\frac{U}{\pi\Delta}\right)^2 z = \sqrt{1 + 4\left(\frac{U}{\pi\Delta}\right)^2\left(3 - \frac{\pi^2}{4}\right)} - 1. \quad (\text{S37})$$

For small U we can therefore use this equation to estimate z , while for large U we use the z obtained either from NRG or from the Bethe ansatz, as outlined in the main text.

Equipped with z for the particle-hole symmetric SIAM on the Keldysh contour, the method of references^{48,55} yields an approximative expression for the renormalized Green function G^x ($x = K, A, R$) of the asymmetric SIAM with energy-dependent hybridization function near the strong-coupling fixed point. Then the imaginary part of G^R can be used to extract the spectral function and calculate the current according to Eqs. S16 and S18. From the resulting conductance $G(V, \theta, B) = dI/dV$, expressions for the expansion coefficients in Eq. (14) of the main manuscript can be constructed. These are obtained as

$$c_B = \frac{(1 - 3\delta^2) \left(1 + \frac{\tilde{u}}{1 + \tilde{\varepsilon}_d^2}\right)^2 + \frac{2\delta\tilde{u}\tilde{\varepsilon}_d(1 + \delta^2)}{(1 + \tilde{\varepsilon}_d^2)^2}}{4(1 + \delta^2)^2}, \quad (\text{S38})$$

$$c_V = \frac{2(3\delta^2 - 1)(\zeta - 1) - (\delta^4 - 1)(2\zeta + 1)\tilde{u}^2 + \frac{4\delta(\delta^2 + 1)\zeta\tilde{u}\tilde{\varepsilon}_d}{(\tilde{\varepsilon}_d^2 + 1)^2}}{2(\delta^2 + 1)^2}, \quad (\text{S39})$$

$$c_{VE_d} = \frac{2(1 - \kappa)\delta}{(\kappa + 1)(\delta^2 + 1)}, \quad (\text{S40})$$

$$c_{\theta V} = \frac{\pi^2}{6(\delta^2 + 1)^4} \left\{ \left(-12(5\delta^4 - 10\delta^2 + 1)(\zeta - 1) + (\delta^2 + 1)\tilde{u}^2 \left(-3\delta^6\zeta + 3\delta^4 \left(\zeta \left(\frac{4\tilde{\varepsilon}_d^2}{(\tilde{\varepsilon}_d^2 + 1)^4} - 7 \right) + 9 \right) \right) \right. \right. \\ \left. \left. + \delta^2 \left(\zeta \left(\frac{8\tilde{\varepsilon}_d^2}{(\tilde{\varepsilon}_d^2 + 1)^4} + 111 \right) - 162 \right) + \zeta \left(-\frac{4\tilde{\varepsilon}_d^2}{(\tilde{\varepsilon}_d^2 + 1)^4} - 15 \right) + 27 \right) - \frac{24\delta(\delta^4 - 1)\tilde{u}\tilde{\varepsilon}_d}{(\tilde{\varepsilon}_d^2 + 1)^2} \right\}, \quad (\text{S41})$$

$$c_{\theta VE_d} = \frac{2\pi^2(\kappa - 1) \left(-3\delta^5\tilde{u}^2(\tilde{\varepsilon}_d^2 + 1)^2 + 6\delta^3(\tilde{u}^2 - 1)(\tilde{\varepsilon}_d^2 + 1)^2 + 3\delta(3\tilde{u}^2 + 2)(\tilde{\varepsilon}_d^2 + 1)^2 + 3\delta^4\tilde{u}\tilde{\varepsilon}_d + 2\delta^2\tilde{u}\tilde{\varepsilon}_d - \tilde{u}\tilde{\varepsilon}_d \right)}{3(\kappa + 1)(\delta^2 + 1)^3(\tilde{\varepsilon}_d^2 + 1)^2}, \quad (\text{S42})$$

$$\delta(\tilde{\epsilon}_d) = \tilde{\epsilon}_d - \tilde{u} \text{Arctan} \tilde{\epsilon}_d, \quad (\text{S43})$$

together with the parameters

$$\begin{aligned} \kappa &= \frac{\Gamma_L}{\Gamma_R}, \\ \zeta &= \frac{3\kappa}{(1+\kappa)^2}. \end{aligned} \quad (\text{S44})$$

Finally, for c_θ we obtain

$$c_\theta = \frac{\pi^2}{3} \frac{1 + 2\tilde{u}^2(1 - \tilde{\delta}^2) + \frac{2\tilde{u}\tilde{\delta}^2}{(1+\tilde{\epsilon}_d^2)^2} - \frac{4\tilde{\delta}^2}{1+\tilde{\delta}^2}}{1 + \tilde{\delta}^2}, \quad (\text{S45})$$

where the quantity $\tilde{\delta}$ appearing in this expression is given by

$$\tilde{\delta} = \tilde{\delta}(\tilde{\epsilon}_d, \tilde{u}) = \tilde{\epsilon}_d - \frac{\tilde{u}}{1+\tilde{u}} \text{Arctan} \tilde{\epsilon}_d. \quad (\text{S46})$$

We note that for particle-hole symmetry ($\tilde{\epsilon}_d = 0$), strong coupling ($\tilde{u} \approx 1$) and $\Gamma_L \ll \Gamma_R$ ($\kappa \approx 0$), we recover the results of Eqs. (S30) and (S31), namely $c_\theta = \pi^2$ and $c_V = 3/2$. Note also that an expansion of the coefficients to lowest order in $(1 - \kappa)$, which corresponds to an expansion around the symmetric coupling case ($\Gamma_L = \Gamma_R$), shows that in this case the 0th order term is non-zero only in c_V and $c_{\theta V}$, the first order term is non-zero only in c_{VE_d} and $c_{\theta VE_d}$, and the second order term is again non-zero only in c_V and $c_{\theta V}$. This odd-even behaviour in the expansions is a consequence of the more general relation $G(\theta, V) = G(\theta, -V)$ valid for $\kappa = 1$, and which combined with Eq. (14) of the main manuscript requires that c_V and $c_{\theta V}$ can only have even powers of $(1 - \kappa)$, while c_{VE_d} and $c_{\theta VE_d}$ can only have odd powers of $(1 - \kappa)$.

References

- [1] J. M. Soler, E. Artacho, J. D. Gale, A. Garcia, J. Junquera, P. Ordejon and D. Sanchez-Portal, *J. Phys.: Condens. Matter*, 2002, **14**, 2745.
- [2] V. Blum, R. Gehrke, F. Hanke, P. Havu, V. Havu, X. Ren, K. Reuter and M. Scheffler, *Comput. Phys. Commun.*, 2009, **180**, 2175.
- [3] X. Ren, P. Rinke, V. Blum, J. Wieferink, A. Tkatchenko, A. Sanfilippo, K. Reuter and M. Scheffler, *New J. Phys.*, 2012, **14**, 053020.
- [4] F. Caruso, P. Rinke, X. Ren, A. Rubio and M. Scheffler, *Phys. Rev. B*, 2013, **88**, 075105.
- [5] A. Droghetti and I. Rungger, *Phys. Rev. B*, 2017, **95**, 085131.
- [6] A. Droghetti, M. Cinchetti and S. Sanvito, *Phys. Rev. B*, 2014, **89**, 245137.
- [7] J. P. Perdew, K. Burke and M. Ernzerhof, *Phys. Rev. Lett.*, 1996, **77**, 3865.
- [8] J. P. Perdew, K. Burke and M. Ernzerhof, *Phys. Rev. Lett.*, 1997, **78**, 1396.
- [9] C. Adamo and V. Barone, *J. Chem. Phys.*, 1999, **110**, 6158.
- [10] A. Tkatchenko and M. Scheffler, *Phys. Rev. Lett.*, 2009, **102**, 073005.
- [11] V. G. Ruiz, W. Liu, E. Zojer, M. Scheffler and A. Tkatchenko, *Phys. Rev. Lett.*, 2012, **108**, 146103.
- [12] A. R. Rocha, V. M. García-Suárez, S. Bailey, C. Lambert, J. Ferrer and S. Sanvito, *Phys. Rev. B*, 2006, **73**, 085414.
- [13] I. Rungger and S. Sanvito, *Phys. Rev. B*, 2008, **78**, 035407.
- [14] N. Marom, *J. Phys.: Condens. Matter*, 2017, **29**, 103003.
- [15] M. L. Mickael L. Perrin, C. J. O. Verzijl, C. A. Martin, A. J. Shaikh, R. Eelkema, J. H. van Esch, J. M. van Ruitenbeek, J. M. Thijssen, H. S. J. van der Zant and D. Dulic, *Nat. Nanotech.*, 2013, **8**, 282.
- [16] X. Lu, M. Grobis, K. H. Khoo, S. G. Louie and M. F. Crommie, *Phys. Rev. B*, 2004, **70**, 115418.
- [17] J. B. Neaton, M. S. Hybertsen and S. G. Louie, *Phys. Rev. Lett.*, 2006, **97**, 216405.
- [18] J. M. Garcia-Lastra, C. Rostgaard, A. Rubio and K. S. Thygesen, *Phys. Rev. B*, 2009, **80**, 245427.
- [19] A. M. Souza, I. Rungger, C. D. Pemmaraju, U. Schwingenschloegl and S. Sanvito, *Phys. Rev. B*, 2013, **88**, 165112.
- [20] S. Y. Quek, H. J. Choi, S. G. Louie and J. B. Neaton, *ACS Nano*, 2011, **5**, 551.
- [21] M. Strange, C. Rostgaard, H. Häkkinen and K. S. Thygesen, *Phys. Rev. B*, 2011, **83**, 115108.
- [22] A. M. Souza, I. Rungger, R. B. Pontes, A. R. Rocha, A. J. Roque da Silva, U. Schwingenschlöegl and S. Sanvito, *Nanoscale*, 2014, **6**, 14495.
- [23] A. Droghetti, P. Thielen, I. Rungger, N. Haag, N. Grossmann, J. Stöckl, M. Stadtmüller, Benjamin Aeschlimann, S. Sanvito and M. Cinchetti, *Nat. Commun.*, 2016, **7**, 12668.

- [24] M. Kepenekian, J.-P. Gauyacq and N. Lorente, *J. Phys.: Condens. Matter*, 2014, **26**, 104203.
- [25] A. Cehovin, H. Mera, J. H. Jensen, K. Stokbro and T. B. Pedersen, *Phys. Rev. B*, 2008, **77**, 195432.
- [26] J. Schrieffer and P. Wolff, *Physical Review*, 1966, **149**, 491.
- [27] P. W. Anderson, *Phys. Rev.*, 1967, **164**, 352–359.
- [28] P. W. Anderson and G. Yuval, *Phys. Rev. Lett.*, 1969, **23**, 89–92.
- [29] P. W. Anderson, G. Yuval and D. R. Hamann, *Phys. Rev. B*, 1970, **1**, 4464–4473.
- [30] G. Yuval and P. W. Anderson, *Phys. Rev. B*, 1970, **1**, 1522–1528.
- [31] K. G. Wilson, *Rev. Mod. Phys.*, 1975, **47**, 773–840.
- [32] A. Hewson, *The Kondo Problem to Heavy Fermions (Cambridge Univ. Press, Cambridge, UK, 1993.*
- [33] N. Andrei and J. H. Lowenstein, *Phys. Rev. Lett.*, 1981, **46**, 356–360.
- [34] H. R. Krishna-murthy, J. W. Wilkins and K. G. Wilson, *Phys. Rev. B*, 1980, **21**, 1003–1043.
- [35] K. G. Wilson, *Phys. Rev. B*, 1971, **4**, 3174–3183.
- [36] K. G. Wilson, *Phys. Rev. B*, 1971, **4**, 3184–3205.
- [37] R. Bulla, T. A. Costi and T. Pruschke, *Rev. Mod. Phys.*, 2008, **80**, 395–450.
- [38] M. H. Hettler, A. N. Tahvildar-Zadeh, M. Jarrell, T. Pruschke and H. R. Krishnamurthy, *Phys. Rev. B*, 1998, **58**, R7475–R7479.
- [39] H. R. Krishna-murthy, J. W. Wilkins and K. G. Wilson, *Phys. Rev. B*, 1980, **21**, 1044–1083.
- [40] R. Bulla, A. Hewson and T. Pruschke, *Journal of Physics: Condensed Matter*, 1998, **10**, 8365.
- [41] R. Žitko, *Phys. Rev. B*, 2011, **84**, 085142.
- [42] W. C. Oliveira and L. N. Oliveira, *Phys. Rev. B*, 1994, **49**, 11986–11994.
- [43] L. Vaugier, A. A. Aligia and A. M. Lobos, *Phys. Rev. B*, 2007, **76**, 165112.
- [44] R. Žitko and T. Pruschke, *Phys. Rev. B*, 2009, **79**, 085106.
- [45] G. D. Mahan, *Many-particle physics*, Springer Science & Business Media, 2013.
- [46] K. Nagaoka, T. Jamneala, M. Grobis and M. F. Crommie, *Phys. Rev. Lett.*, 2002, **88**, 077205.
- [47] A. C. Hewson, *Phys. Rev. Lett.*, 1993, **70**, 4007.
- [48] E. Muñoz, C. J. Bolech and S. Kirchner, *Phys. Rev. Lett.*, 2013, **110**, 016601.
- [49] T. A. Costi, A. C. Hewson and V. Zlatić, *J. Phys.: Cond. Matt.*, 1994, **6**, 2519.
- [50] K. Nagaoka, T. Jamneala, M. Grobis and M. F. Crommie, *Phys. Rev. Lett.*, 2002, **88**, 077205.
- [51] Y. Meir and N. S. Wingreen, *Phys. Rev. Lett.*, 1992, **68**, 2512–2515.
- [52] P. Nozières, *Journal of Low Temperature Physics*, 1974, **17**, 31.
- [53] D. Goldhaber-Gordon, J. Gores, M. A. Kastner, H. Shtrikman, D. Mahalu and U. Meirav, *Phys. Rev. Lett.*, 1998, **81**, 5225.
- [54] L. Merker, S. Kirchner, E. Muñoz and T. A. Costi, *Phys. Rev. B*, 2013, **87**, 165132.
- [55] E. Muñoz, F. Zamani, L. Merker, T. A. Costi and S. Kirchner, *J. Phys.: Conf. Ser.*, 2017, **807**, 092001.